

## Supporting Information

### **Conversion reaction mechanism of bimetallic Ni-Fe hydroxycarbonate and its encapsulation in carbon nanospheres for achieving excellent Li-ion storage performance**

Jin-Sung Park<sup>†</sup>, Jeong Hoo Hong<sup>†</sup>, Su Hyun Yang, and Yun Chan Kang<sup>\*</sup>

Department of Materials Science and Engineering, Korea University, Anam-Dong, Seongbuk-Gu, Seoul 136-713, Republic of Korea.

[<sup>†</sup>] These two authors contributed equally to this work.

<sup>\*</sup>Corresponding author. E-mail: yckang@korea.ac.kr (Yun Chan Kang, Fax: (+82) 2-928-3584)

## Experimental Section (Continued)

### *Characterization Techniques*

The morphological characteristics of a-NiFeHC and c-NiFeHC were examined with field emission scanning electron microscopy (FE-SEM; Hitachi, S-4800) and transmission electron microscopy (FE-TEM; JEOL, JM-2100F). The chemical nature of NiFe(OH)(CO<sub>3</sub>) samples were characterized by X-ray photoelectron spectroscopy (XPS; Thermo Scientific K-Alpha™) with focused monochromatic Al-K<sub>α</sub> radiation (12 kV and 20 mA). Ex-situ TEM and XPS results were obtained by discharging and charging until the preselected potentials were reached with the same apparatus. The crystal phases of the synthesized samples were analyzed with X-ray diffraction (XRD; X'Pert PRO MPD) using Cu K<sub>α</sub> radiation ( $\lambda = 1.5418 \text{ \AA}$ ) at Korea Basic Science Institute (Daegu Centre). To ascertain the types of chemical bonding present in Ni Fe hydroxycarbonate material, Fourier transform infrared (FT-IR) spectroscopy were obtained with JASCO FT-IR 480 Plus spectrophotometer. Thermogravimetric analysis (TGA) was carried out from 25 to 800 °C in air atmosphere using Pyris 1 TGA (Perkin Elmer) with 10 °C min<sup>-1</sup> ramping rate. The porosity characteristics of the synthesized samples were analyzed with Brunauer-Emmett-Teller (BET) method using N<sub>2</sub> as the adsorbate gas.

### *Electrochemical measurements*

The electrochemical performances of the samples were analyzed using 2032-type lithium ion half cells. The electrodes were prepared from slurry process; active anode material, carbon black, and sodium carboxymethyl cellulose (CMC) binder were homogeneously mixed in 7:2:1 weight ratio and applied onto copper foil. The prepared electrodes were dried in vacuum oven and then were punched at the time of cell fabrication to obtain a circular electrode with dimension of 1.4 cm × 1.4 cm and mass loading of 1.2 mg cm<sup>-2</sup>. Microporous

poly(propylene) film and lithium metal disc were adopted as the separator and counter electrode, respectively. The electrolyte used in this study was 1 M LiPF<sub>6</sub> salt dissolved in a mixed solution of fluoroethylene carbonate and dimethyl carbonate (FEC/DMC) in a 1:1 volume ratio. The half-cell was assembled in a glove box filled with Ar gas and went through various electrochemical tests. The cycle and rate performances were analyzed from galvanostatic discharge and charge processes in a voltage range of 0.001-3.0 V at various current densities. Cyclic voltammograms were obtained in the same voltage range at various scan rates. In-situ and ex-situ electrochemical impedance spectra (EIS) of the samples were analyzed in the frequency range of 0.01 Hz to 100 kHz. During in situ EIS analysis, the cell was galvanostatically cycled at a current density of 0.1 A g<sup>-1</sup>, and the Nyquist plots were obtained at preselected potentials.

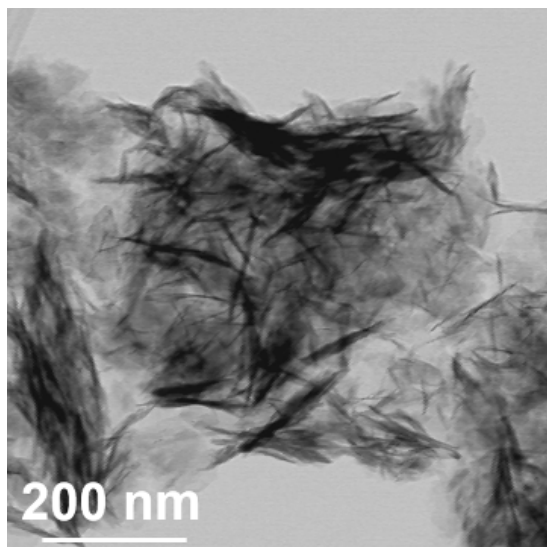


**Fig. S1** The original photo of the scanned region in Fig. 1d.

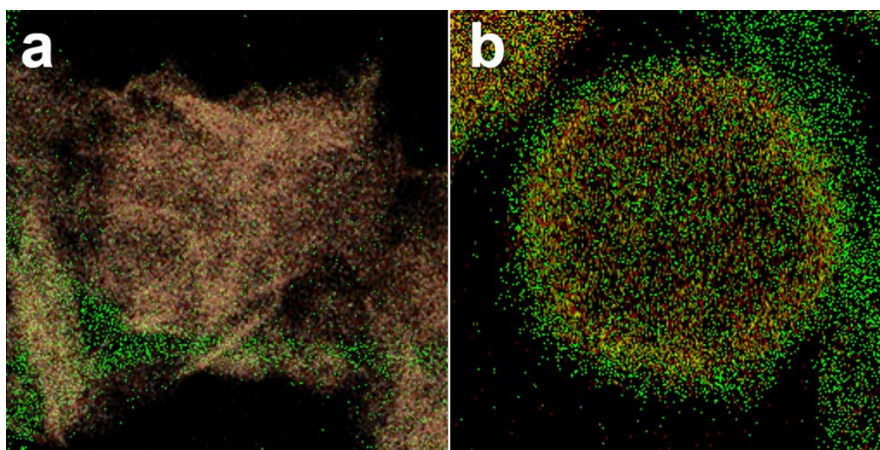


**Fig. S2** The overlapped elemental mapping images of (a) c-NiFeHC and (b) a-NiFeHC@C.  
(Ni: yellow, Fe: red, O: grey, C: green)

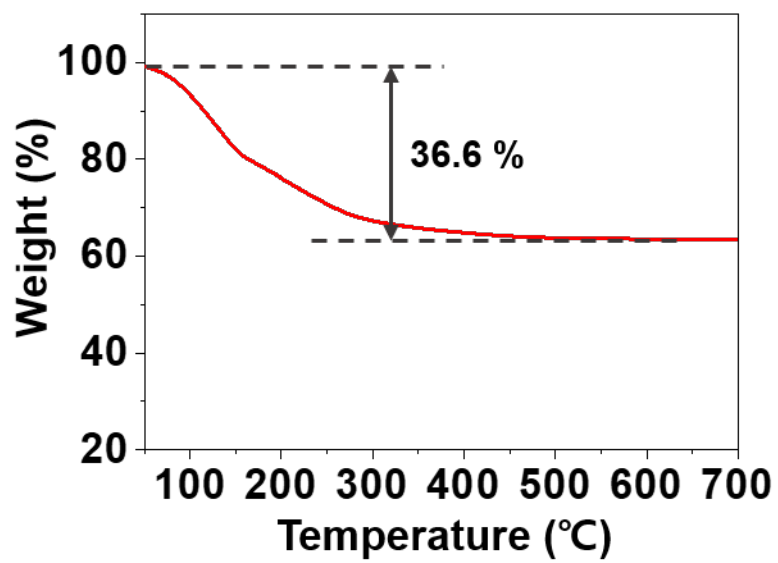


**Fig. S3** TGA curve of c-NiFeHC.

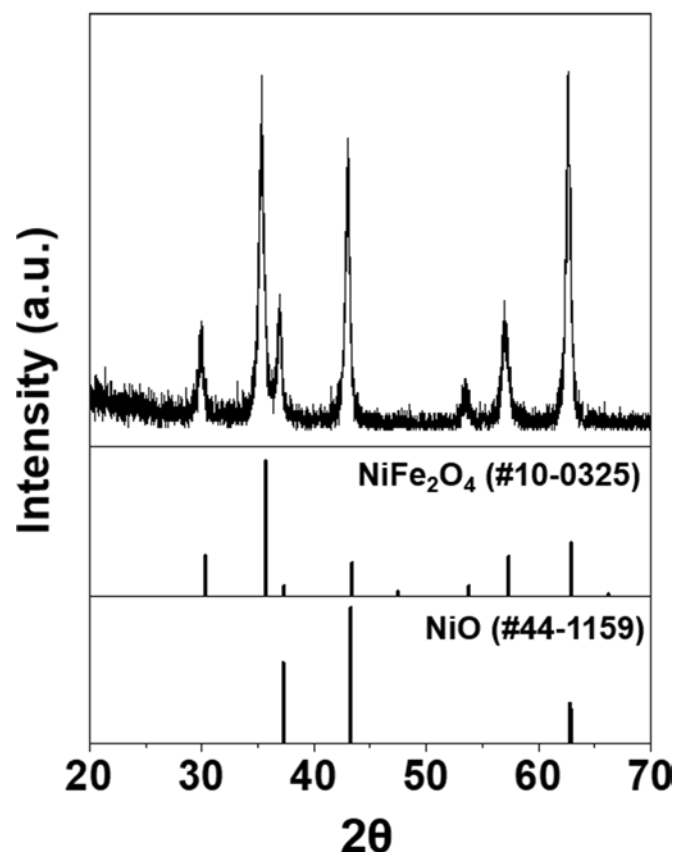


**Fig. S4** XRD pattern of of c-NiFeHC that underwent TGA measurement.

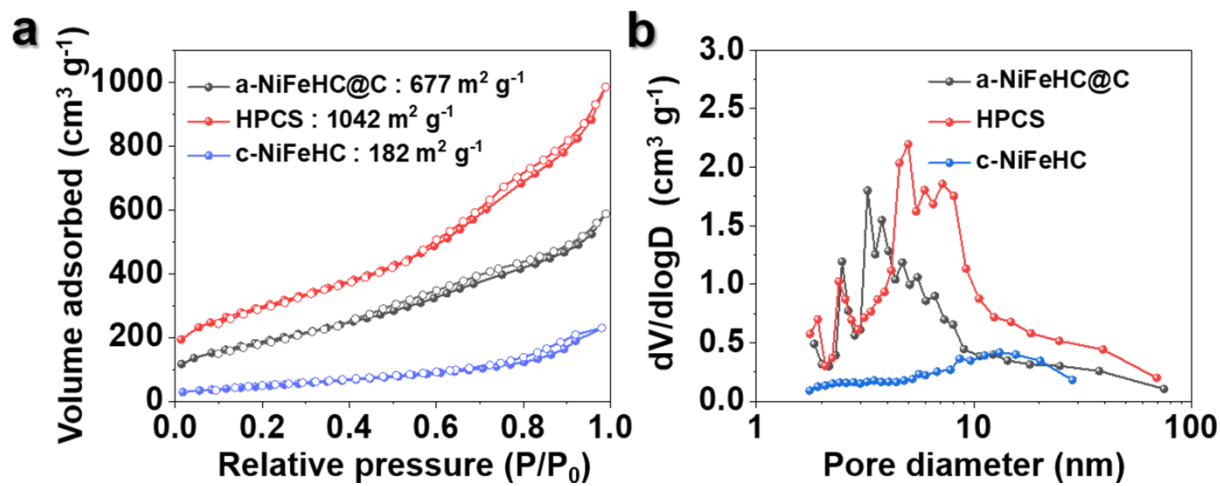


**Fig. S5** (a)  $N_2$  gas adsorption and desorption isotherms and (b) BJH pore size distributions of HPCS, c-NiFeHC, and a-NiFeHC@C.

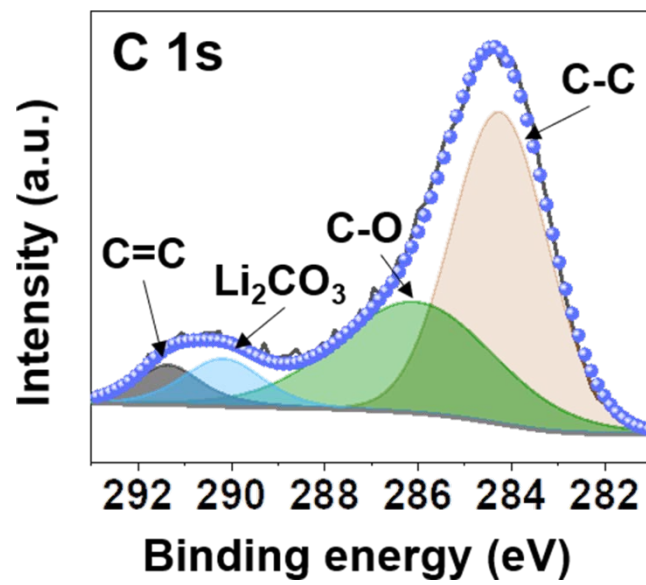
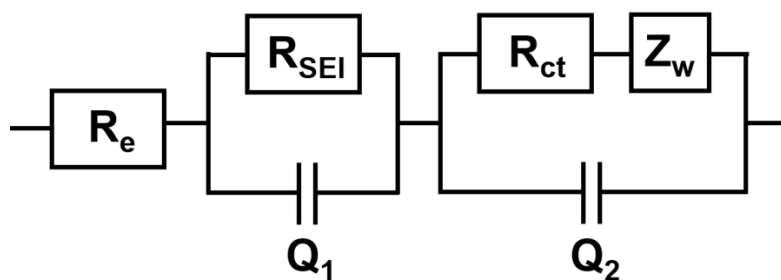


**Fig. S6** C 1s ex-situ XPS spectra for the discharged state (c-NiFeHC).



$R_e$ : the electrolyte resistance, corresponding to the intercept of high frequency semicircle at

$Z_{re}$  axis

$R_{SEI}$ : SEI material-related resistance corresponding to the high-frequency semicircle

$Q_1$ : dielectric relaxation capacitance corresponding to the high-frequency semicircle

$R_{ct}$ : charge transfer resistance related to the middle-frequency semicircle

$Q_2$ : the double-layer capacitance related to the middle-frequency semicircle

$Z_w$ : the Li-ion diffusion resistance

**Fig. S7** Randle-type equivalent circuit model used for EIS fitting.

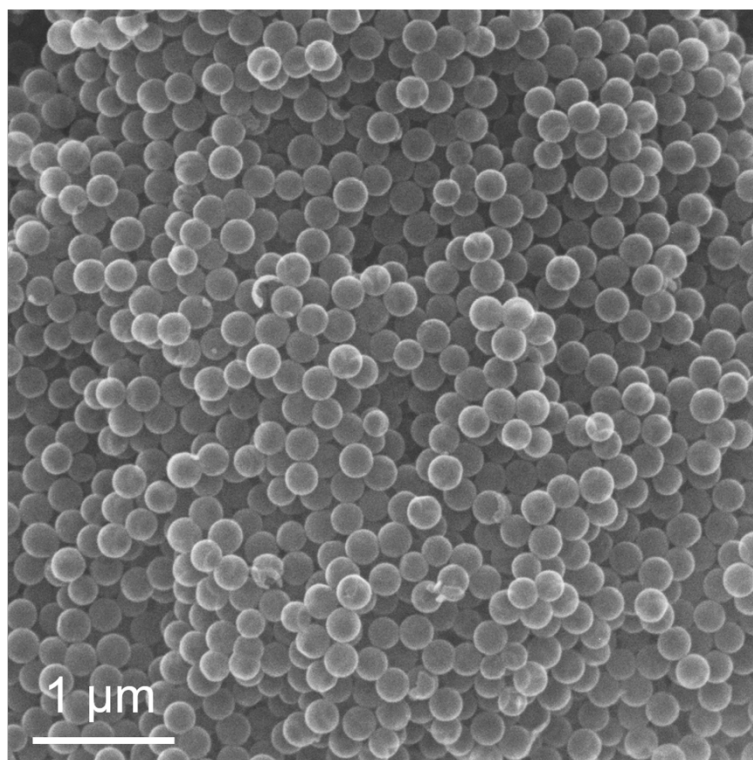


**Fig. S8** SEM image of unimodal HPCS.

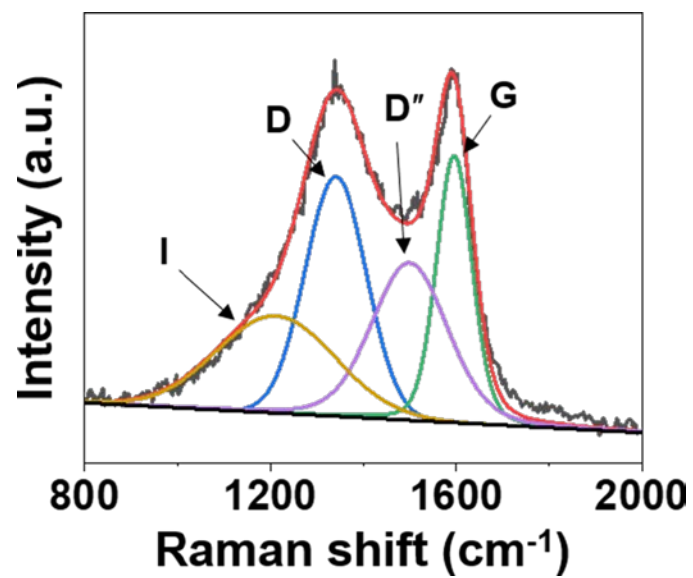


**Fig. S9** Raman spectrum of hollow and porous-walled carbon spheres.

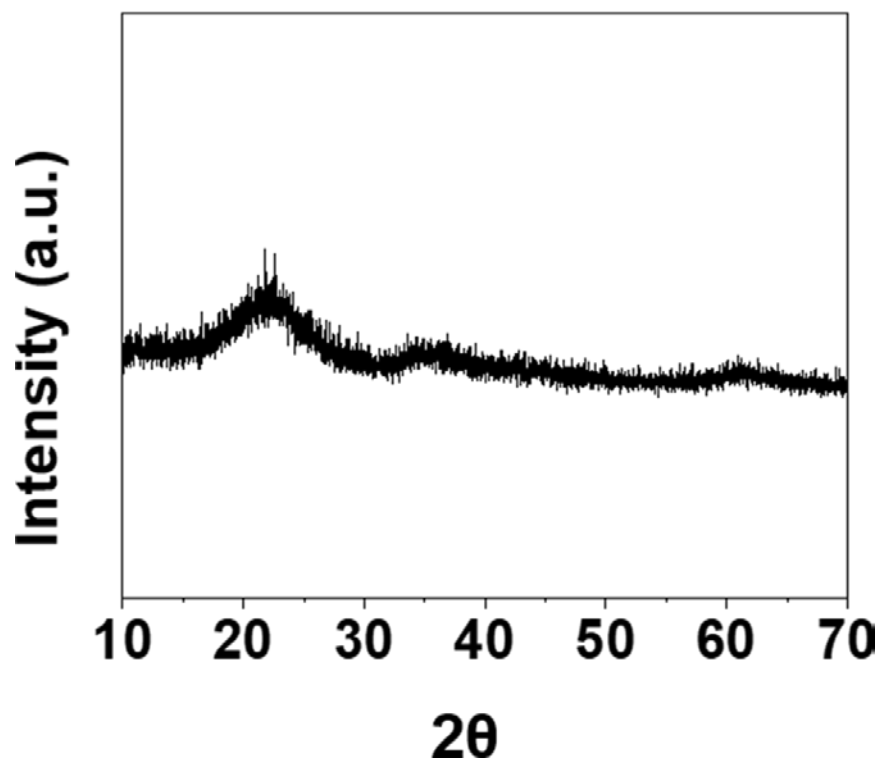


**Fig. S10** XRD pattern of a-NiFeHC@C.

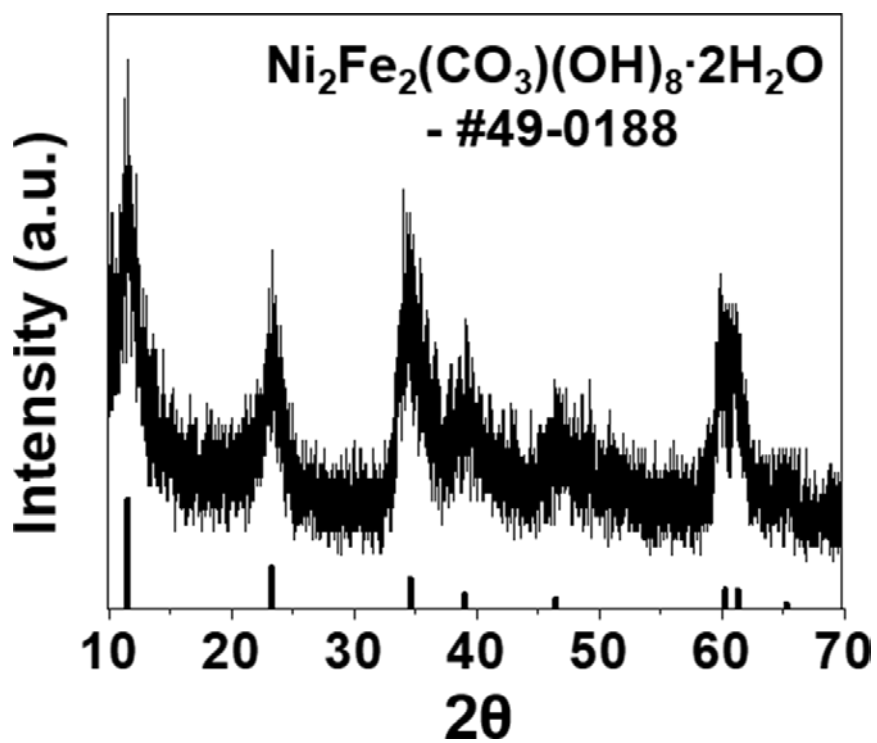


**Fig. S11** The XRD pattern of NiFeHC material synthesized from instant reaction between aqueous solution containing Fe and Ni metal salts and aqueous  $\text{Na}_2\text{CO}_3$  solution.

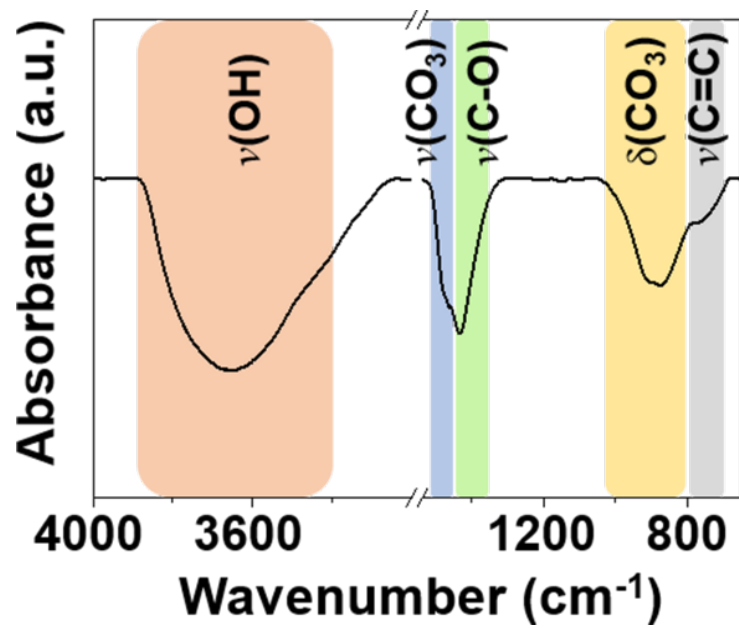


**Fig. S12** FT-IR spectrum of a-NiFeHC@C.

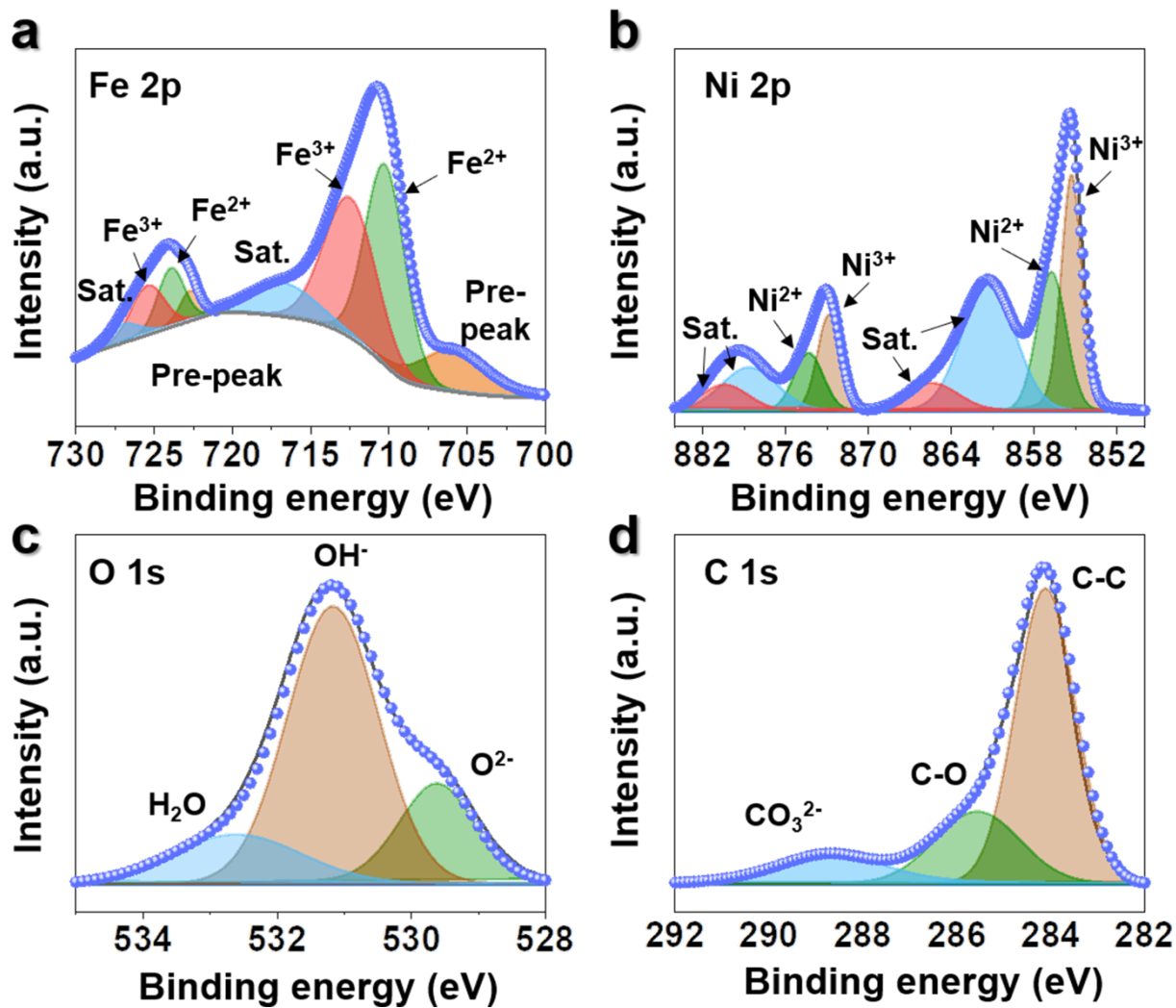
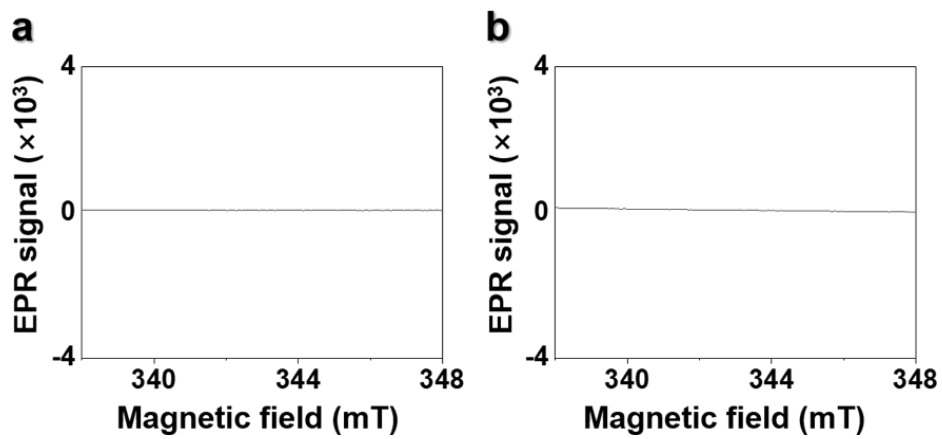
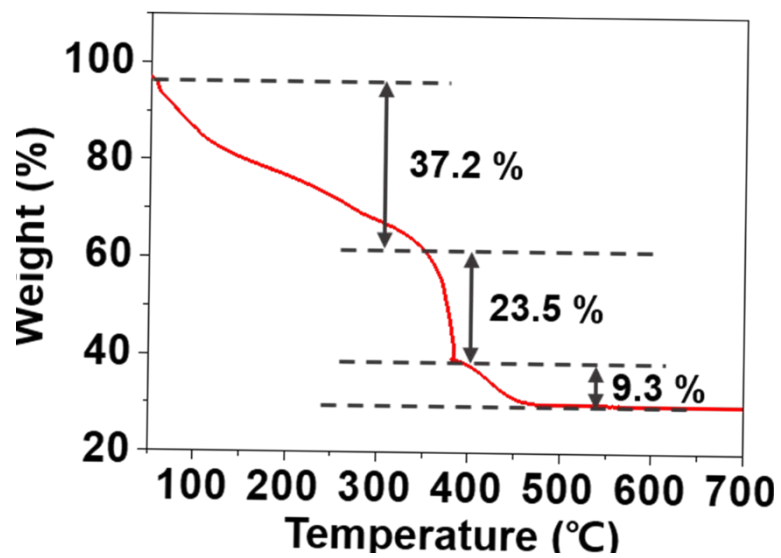


Fig. S13 (a) Fe 2p, (b) Ni 2p, (c) O 1s, (d) C 1s XPS spectra of a-NiFeHC@C.



**Fig. S14** EPR spectra of (a) a-NiFeHC@C and (b) c-NiFeHC.



**Fig. S15** TGA curve of a-NiFeHC@C.

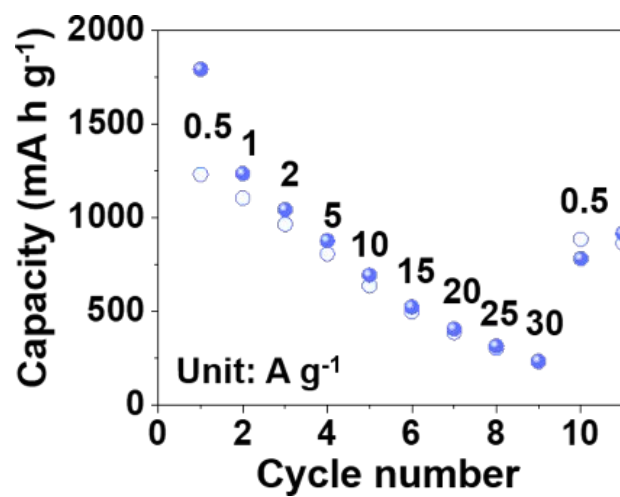


**Fig. S16** Rate performance of c-NiFeHC (one cycle for each current density).

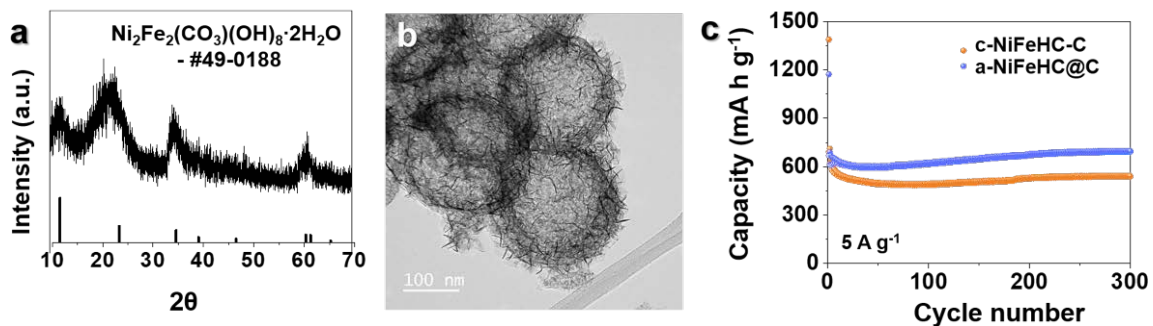


**Fig. S17** (a) XRD pattern and (b) TEM image of NiFeHC material synthesized from 6 h precipitation reaction between solution containing Fe and Ni metal salts and  $\text{Na}_2\text{CO}_3$  aqueous solution (c-NiFeHC-C). (c) cycle performance comparison between a-NiFeHC and c-NiFeHC-C at  $0.5 \text{ A g}^{-1}$ .

**Table S1.** Electrochemical properties of various metal carbonates, hydroxides, and hydroxycarbonates applied as lithium-ion batteries reported in the previous literatures.

Materials	Voltage range (V)	Current rate	Discharge capacity [mA h g <sup>-1</sup> ] and (cycle number)	Rate capacity [mA h g <sup>-1</sup> ] (current rate)	Ref
Sheet-stacking Ni(OH) <sub>2</sub> /graphene composite	0.001-3.0	0.1 A g <sup>-1</sup>	1132 (100)	687 (2.0 A g <sup>-1</sup> )	[1]
Nanoflake Ni(OH) <sub>2</sub> decorating reduced graphene oxide platelets	0.005-3.0	0.1 A g <sup>-1</sup>	1003 (40)	779 (1.6 A g <sup>-1</sup> )	[2]
Graphene coated large-area Co(OH) <sub>2</sub> heterostructures	0.01-3.0	0.058 A g <sup>-1</sup>	706 (50)	220 (1.16 A g <sup>-1</sup> )	[3]
Polypyrrole coated urchin-like CoCO <sub>3</sub> microspheres	0.01-3.0	0.1 A g <sup>-1</sup>	1071 (100)	671 (2.0 A g <sup>-1</sup> )	[4]
Acanthosphere FeCO <sub>3</sub>	0.01-3.0	0.1 A g <sup>-1</sup>	587 (100)	238 (10.0 A g <sup>-1</sup> )	[5]
MnCO <sub>3</sub> nanoplatelets-RGO composites	0.01-3.0	0.1 A g <sup>-1</sup>	872 (200)	278 (2.0 A g <sup>-1</sup> )	[6]
Co <sub>2</sub> (OH) <sub>2</sub> CO <sub>3</sub> nanosheets	0.01-3.0	1.0 A g <sup>-1</sup>	400 (200)	323 (2.0 A g <sup>-1</sup> )	[7]
Sandwich-like Co(CO <sub>3</sub> ) <sub>0.5</sub> (OH)/graphene composite	0.001-3.0	1.0 A g <sup>-1</sup>	611 (300)	469 (2.0 A g <sup>-1</sup> )	[8]
Zn <sub>5</sub> (CO <sub>3</sub> ) <sub>2</sub> (OH) <sub>6</sub> with unique flaky morphology	0.02-3.0	0.094 A g <sup>-1</sup>	299 (100)	-	[9]
<b>Amorphous NiFeHC/carbon composite</b>	<b>0.001-3.0</b>	<b>1.0 A g<sup>-1</sup></b>	<b>1023 (150)</b>	<b>251 (30.0 A g<sup>-1</sup>)</b>	<b>This work</b>

## References

- [1] Z. Zhai, Q. Liu, Y. Zhu, J. Cao and S. Shi, *J. Alloys Compd.*, 2019, **775**, 1316-1323.
- [2] X. Zhu, Y. Zhong, H. Zhai, Z. Yan and D. Li, *Electrochim. Acta*, 2014, **132**, 364-369.
- [3] X. L. Huang, J. Chai, T. Jiang, Y. J. Wei, G. Chen, W. Q. Liu, D. Han, L. Niu, L. Wang and X. B. Zhang, *J. Mater. Chem.*, 2012, **22**, 3404-3410.
- [4] Z. Ding, B. Yao, J. Feng and J. Zhang, *J. Mater. Chem. A*, 2013, **1**, 11200-11209.
- [5] X. Feng, Q. Shen, Y. Shi and J. Zhang, *Ceram. Int.*, 2016, **42**, 14246-14251.
- [6] K. Wang, Y. H. Shi, H. H. Li, H. F. Wang, X. Y. Li, H. Z. Sun, X. L. Wu, H. M. Xie, J. P. Zhang and J. W. Wang, *Electrochim. Acta*, 2016, **215**, 267-275.
- [7] X. Zhou, Y. Zhong, M. Yang, Q. Zhang, J. Wei and Z. Zhou, *ACS Appl. Mater. Interfaces*, 2015, **7**, 12022-12029.
- [8] S. Shi, M. Zhang, Y. Liu and G. Yang, *J. Alloys Compd.*, 2018, **764**, 709-717.
- [9] W. Han, K. Yang, D. Li, Z. Zhang, J. Ma, S. Ni and X. Yang, *Mater. Lett.*, 2016, **164**, 148-151.

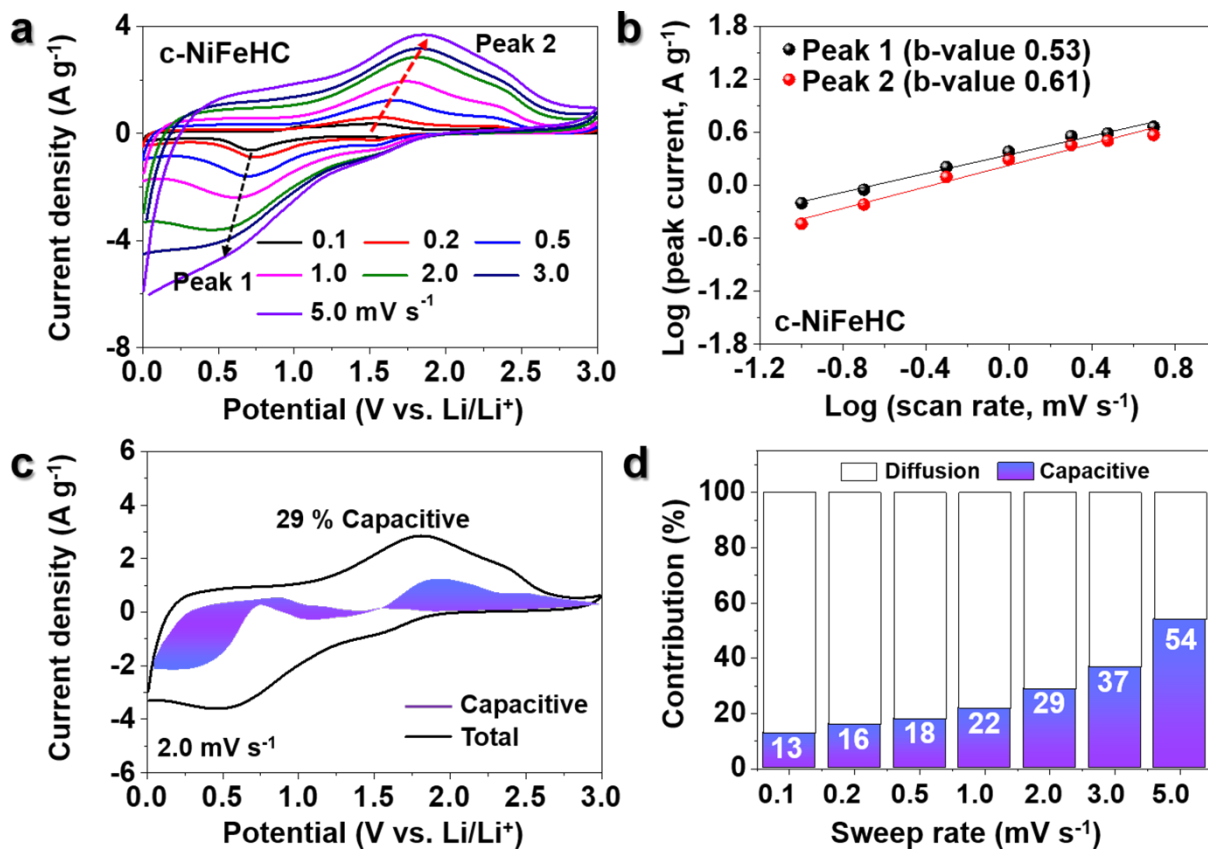


**Fig. S18** (a) Cyclic voltammograms of c-NiFeHC at various sweep rates, (b) fitted log (peak current) vs. log (scan rate) for Peak 1 and Peak 2 corresponding to the main anodic and cathodic peaks, respectively, (c) cyclic voltammogram that show capacitive current (colored area) to the total current, and (d) percentage of capacity contribution at varying sweep rates.

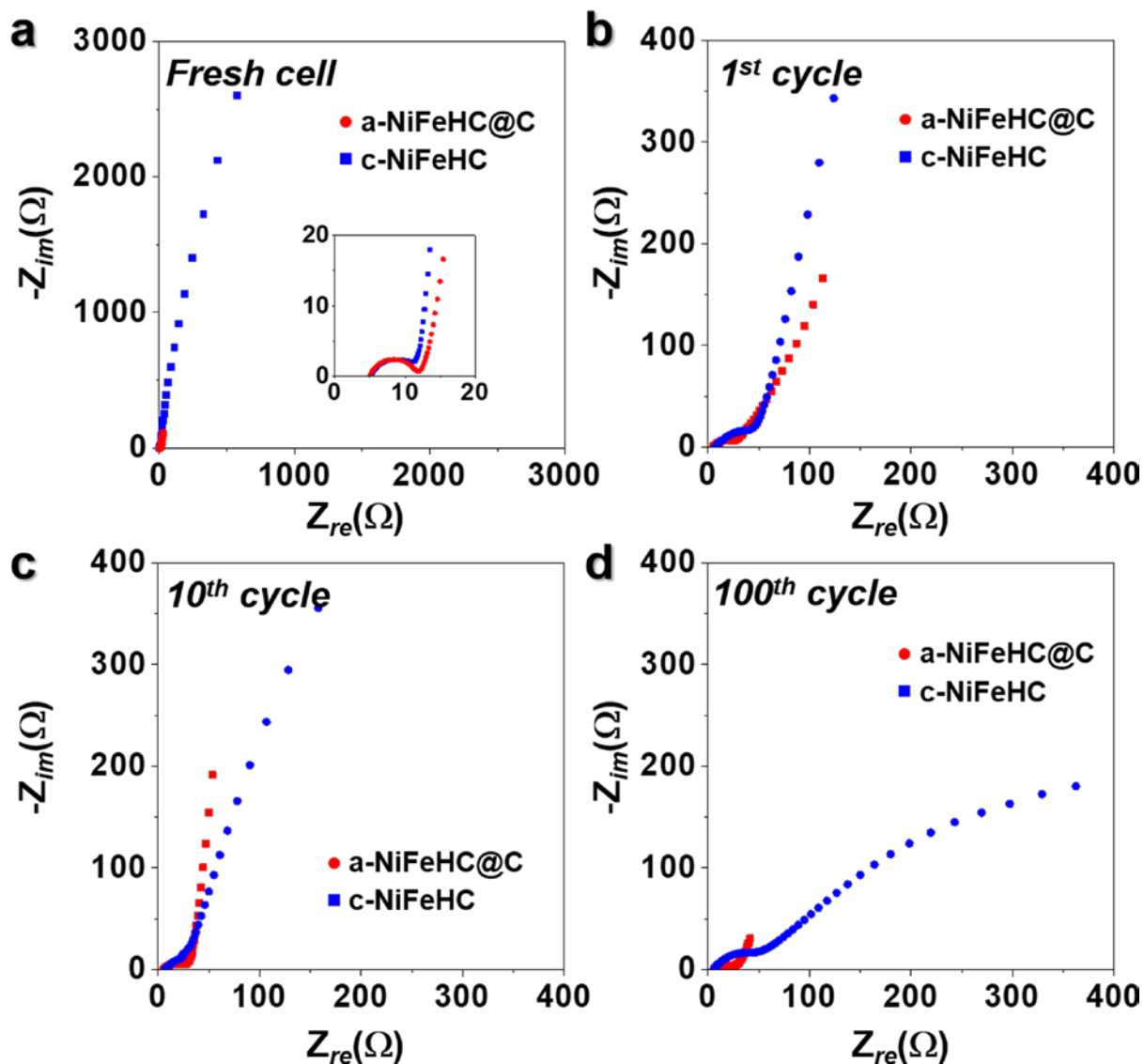


**Fig. S19** Ex-situ Nyquist plots of a-NiFeHC@C and c-NiFeHC (a) before cycling and after the (b) 1<sup>st</sup>, (c) 10<sup>th</sup>, (d) 100<sup>th</sup> cycles.

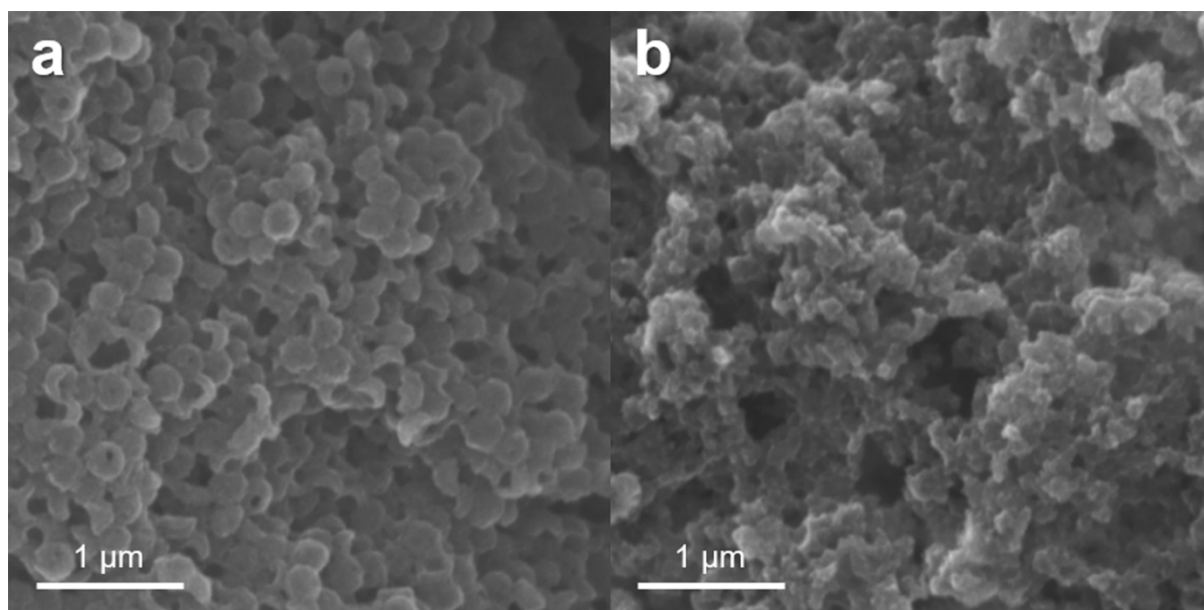


**Fig. S20** SEM images of (a) a-NiFeHC@C and (b) c-NiFeHC after 100 cycles.

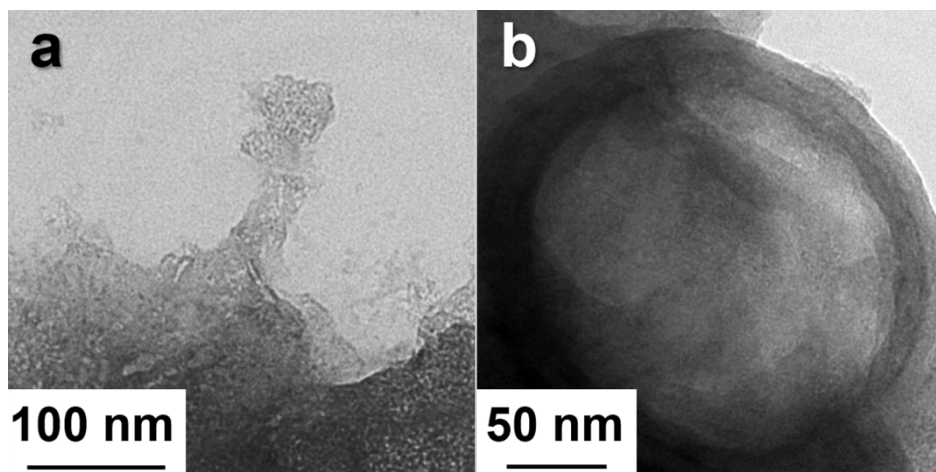


**Fig. S21** TEM image of (a) c-NiFeHC and (b) a-NiFeHC@C after 100 cycles.